Journal of Physics Communications

PAPER • **OPEN ACCESS**

Bi_2Se_3 topological insulator quantum wires

To cite this article: A Nikolic and C H W Barnes 2018 *J. Phys. Commun.* **2** 095007

View the article online for updates and enhancements.

This content was downloaded from IP address 131.111.184.102 on 12/11/2018 at 15:04

Journal of Physics Communications

PAPER

Bi_2Se_3 topological insulator quantum wires

A Nikolic and C H W Barnes

Cavendish Laboratory, Department of Physics, University of Cambridge, Cambridge CB3 0HE, United Kingdom

E-mail: an340@cam.ac.uk

Keywords: topological insulators, 2D, 4 band model, ballistic conduction, bismuth selenide, finite difference

OPEN ACCESS

RECEIVED
4 March 2018

REVISED
10 July 2018

ACCEPTED FOR PUBLICATION
13 August 2018

PUBLISHED
5 September 2018

Original content from this work may be used under the terms of the Creative Commons Attribution 3.0 licence.

Any further distribution of this work must maintain attribution to the author(s) and the title of the work, journal citation and DOI.

Abstract

We study the effect of 3D topological insulator contributions to the band structure and wavefunctions of quasi-one-dimensional electron systems. Our model for this system consists of an effective Hamiltonian derived previously in the literature from the crystal symmetries of Bi_2Se_3. We find that in wires whose face lies in the plane formed by the y and z crystal directions and whose width is around 25 quintuple layers or more, the bands nearest to the gap are non-monotonic; we show that this has implications for the conductance of the wire. In addition, we observed increasing penetration depth of surface states with increasing wavenumber of the propagating mode. We believe these results have qualitative relevance to the family of 3D topological insulators whose crystal structure is characterised by the space group D_{3d}^5, and that the work done here contributes to the wider field of the study of conductance in topological insulators.

1. Introduction

Topological insulators (TIs) are a recently identified quantum state of matter with bulk states characteristic of semiconductors or insulators and conducting gapless surface states characteristic of a Dirac metal with strong Rashba-like spin–orbit coupling [1–4]. Recent advances in the growth of thin-film ultra high quality topological insulator material promise to enrich the physics of quantum wires through the introduction of a number of topology-related phenomena. Such thin films of TIs have been the subject of recent study for the purposes of determining the relationship between the bulk and surface states [5–7]. Quantum wires fabricated from gated or etched thin-film TI material will have two inequivalent perpendicular surfaces. The physics of these systems combines quantised surface conduction of Dirac electrons or holes, with Klein tunnelling between inequivalent surfaces, spin–orbit coupling effects and electron-electron interactions. In this paper we will not consider electron-electron interaction effects directly, other than by admitting that there will be some form of lateral effective potential. We will concentrate on a specific, well known, TI Bi_2 Se_3 that has bulk states with a semiconducting gap arising from single-particle band structure effects and three inequivalent surfaces in the x, y and z directions [8–12]. Our results are therefore specific to this material but they will be observable to some degree in any TI material, especially those where interaction effects are weak and the material has a single Dirac cone. Examples of similar approaches to that taken in this work can be found in [13, 14], amongst many others.

Topological insulator wires have seen much study experimentally and theoretically. The Aharonov-Bohm effect in topological nanowires was carefully studied in [15]. Bi_2Se_3 nanowires have been studied as field-effect transistors [16]; there has also been considerable interest in the presence of Majorana modes in TI wires [17]. More recently, work has been done specifically in the area of disordered quantum wires (see [18–20]). The model Hamiltonian used throughout the paper, an effective four-band continuum Hamiltonian previously used to capture the fundamental physics of surface states in TIs, has also seen considerable study [21–28]. This model is presented in section 2. Also in section 2, we quantise 2 components of the wavevector $\mathbf{k}$, discuss the discretization of the problem to make it suitable for numerical computation and formulate the corresponding Hamiltonian and spin operators. We present our results in section 3, where we explain the physical origin of our dispersion relations and eigenstates. The band structure is used to calculate the ballistic conductance of a long Q1DES. Conclusions are made in section 4.

© 2018 The Author(s). Published by IOP Publishing Ltd

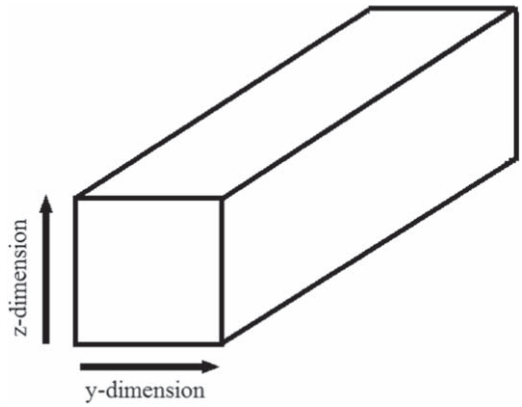

Figure 1. Illustration of the generic Bi_2Se_3 device being studied in most of these results, with specific dimensions given in each figure.

Table 1. Table of parameters used in program obtained by Liu *et al* [29] using $\mathbf{k}\cdot\mathbf{p}$ theory.

	Bi_2Se_3
A_0/eVÅ	3.33
B_0/eVÅ	2.26
C_0/eV	−0.0083
C_1/eV Å^2	5.74
C_2/eV Å^2	30.4
M_0/eV	−0.28
M_1/eV Å^2	6.86
M_2/eV Å^2	44.5

2. Model

For this work, we use the Hamiltonian presented by Liu *et al* [29], which has its origin in a tight binding model of the hybridized and spin-split Bi and Se *p*-orbitals, as well as the symmetries of the crystal. Here we retain only terms up to k^2; thus we arrive at the following effective Hamiltonian:

$$\hat{\mathcal{H}}_{\text{eff}} = \hat{\mathcal{H}}_0 + V(r)\mathbb{I} \tag{1}$$

$$\hat{\mathcal{H}}_0 = \epsilon_{\mathbf{k}}\mathbb{I} + M(\mathbf{k})\Gamma_5 + B_0\Gamma_4 k_z + A_0(\Gamma_1 k_y - \Gamma_2 k_x) \tag{2}$$

where $\mathbb{I}$ is the 4×4 identity matrix, $\epsilon_{\mathbf{k}} = C_0 + C_1 k_z^2 + C_2 k_\parallel^2$, $M(\mathbf{k}) = M_0 + M_1 k_z^2 + M_2 k_\parallel^2$, and $k_\parallel^2 = k_x^2 + k_y^2$. The constants used in these defintions are defined in table 1. Γ_i $(1 \leqslant i \leqslant 5)$ represent the 4×4 Dirac matrices, and $V(y, z)$ is zero in the simulation domain and infinite at its edges. We present the derivation and atomic origin of this Hamiltonian in appendix A.

Figure 1 illustrates the device that we apply this Hamiltonian to. In order to apply the Hamiltonian (1) to a finite system instead of the infinite system limit, the substitutions $k_z \to -\mathrm{i}\partial_z$ and $k_y \to -\mathrm{i}\partial_y$ are made in the Schrödinger equation

$$\hat{\mathcal{H}}_{\text{eff}}\mathbf{\Phi}(y, z) = E\mathbf{\Phi}(y, z), \tag{3}$$

representing quantisation in the z and y directions respectively. The stationary states of the system are denoted by $\mathbf{\Phi}(y, z)$, and the components with respect to the basis of the Hamiltonian by $\{\phi_i(y, z)\}$ $(1 \leqslant i \leqslant 4)$ which depend only on y and z by virtue of the system's translational invariance in the x direction. Equation (3) then becomes

$$\left(\mathcal{H}'(k_x, y, z) + \sum_j (\mathcal{H}_1^{(j)}\partial_j + \mathcal{H}_2^{(j)}\partial_j^2)\right)\mathbf{\Phi}(y, z) = 0, \tag{4}$$

where

$$\mathcal{H}'(k_x, y, z) = \mathcal{H}_0(k_x) + V(y, z)\mathbb{I}, \tag{5}$$

the index $j = y, z$ and the matrices $\mathcal{H}_0(k_x)$ and $\mathcal{H}_i^{(j)}$ may be found in equations (28) to (32). We solve equation (4) on the surface $\mathcal{S}$ defined w.l.o.g. by $x = 0$, and $0 \leqslant y \leqslant L$, $0 \leqslant z \leqslant L$. We impose Dirichlet boundary conditions that $\Phi = 0$ on $\partial\mathcal{S}$, the boundary of $\mathcal{S}$, since the potential V is set to be infinite outside the wire. The surface is split up into $(n + 1) \times (n + 1)$ lattice sites, separated by a distance $h = L/(n + 1)$ in both y and z. We then substitute the z- and y- derivatives for (central) finite difference operators with step length h [30] (defined in the appendix)to produce n^2 sets of 4 coupled equations for $\{\phi_i\}$ at each site lattice site of the form

$$\sum_{\mu=-1}^{1}\sum_{\nu=-1}^{1} \mathcal{C}_{\mu,\nu}\Phi_{i+\mu,j+\nu} = 0 \tag{6}$$

where $\Phi_{i,j} = (\phi_1(y_i, z_j), \ldots, \phi_4(y_i, z_j))^T$ and the 4×4 matrices $\mathcal{C}_{\mu,\nu}$ can be found in equations (33) to (35). $\mathcal{C}_{\mu,\nu} = \mathsf{0}$ if both μ and ν are nonzero. The boundary conditions on $\partial\mathcal{S}$ give us that $\Phi_{0,j} = \Phi_{n+1,j} = \Phi_{i,0} = \Phi_{i,n+1} = 0$. The equations may then be written as an ($4n^2$-dimensional) eigenvalue problem

$$\mathsf{H}\Phi^{(i)} = E_i\Phi^{(i)}. \tag{7}$$

$\mathcal{C}_{\mu,0} = \mathcal{C}^{\dagger}_{-\mu,0}$ and $\mathcal{C}_{0,\nu} = \mathcal{C}^{\dagger}_{0,-\nu}$. so $\mathsf{H} = \mathsf{H}^{\dagger}$ is a sparsely populated Hermtian band matrix, which gives rise to *real* eigenenergies as required. The z index (1 to n) of the ith element of Φ is given by $\lfloor i/4 \rfloor/n + 1$ and the y index by $\mathrm{mod}(\lfloor i/4 \rfloor, n) + 1$. Numerical methods were used to find the eigenvalues and eigenvectors of the Hamiltonian matrix H [31], which we denote as E_i and $\Phi^{(i)}$ respectively.

The same procedure can be carried out with the substitutions $k_x \to -\mathrm{i}\partial_x$ and $k_y \to -\mathrm{i}\partial_y$ such that the wire lies instead along the $\hat{\mathbf{z}}$ direction, and the surface over which we solve, $\mathcal{S}'$, lies in the x-y plane. We still obtain n^2 sets of 4 simultaneous equations similar to (6), but the matrices are now given by $\mathcal{C}'_{\mu,\nu}$. The states are labelled as $|\Phi'^{(i)}\rangle$ with energies E'_i. We expect the states to exhibit more symmetry due to the symmetry between k_x and k_y in the model Hamiltonian (2) as $k_{\|}$ is invariant under the transformation $k_x \leftrightarrow k_y$. Naturally, we should also be able to substitute $k_x \to -\mathrm{i}\partial_x$ and $k_z \to -\mathrm{i}\partial_z$ to produce results similar to the case where we quantise in y and z, but in this work we restrict ourselves to the y-z and x-y planes.

Within this model we also consider the action of the total angular momentum operators $\hat{J}_{x(yz)}$. Projecting the total momentum operators onto the eigenbasis of the Hamiltonian ($|P1^+_-, \pm\frac{1}{2}\rangle, |P2^-_+, \pm\frac{1}{2}\rangle$) which are also the eigenstates of $\hat{J}_z$, we obtain

$$\mathsf{j}_x = \begin{pmatrix} 0 & 0 & \frac{1}{2} & 0 \\ 0 & 0 & 0 & \frac{1}{2} \\ \frac{1}{2} & 0 & 0 & 0 \\ 0 & \frac{1}{2} & 0 & 0 \end{pmatrix}, \quad \mathsf{j}_y = \begin{pmatrix} 0 & 0 & -\frac{\mathrm{i}}{2} & 0 \\ 0 & 0 & 0 & -\frac{\mathrm{i}}{2} \\ \frac{\mathrm{i}}{2} & 0 & 0 & 0 \\ 0 & \frac{\mathrm{i}}{2} & 0 & 0 \end{pmatrix},$$

$$\mathsf{j}_z = \begin{pmatrix} \frac{1}{2} & 0 & 0 & 0 \\ 0 & \frac{1}{2} & 0 & 0 \\ 0 & 0 & -\frac{1}{2} & 0 \\ 0 & 0 & 0 & -\frac{1}{2} \end{pmatrix}. \tag{8}$$

As shown, $\mathsf{j}_x = \frac{1}{2}\sigma_x \otimes 1$, $\mathsf{j}_y = \frac{1}{2}\sigma_y \otimes 1$ and $\mathsf{j}_z = \frac{1}{2}\sigma_z \otimes 1$, where $\{\sigma_i\}$ are the Pauli spin matrices and $\otimes$ is the matrix direct (Kronecker) product. Using the fact that $\langle\Phi|\hat{J}_{x(yz)}|\Phi\rangle \to \sum_i\sum_j \Phi^{\dagger}_{i,j}\mathsf{j}_{x(yz)}\Phi_{i,j} \equiv \Phi^{\dagger}\mathsf{J}_{x(yz)}\Phi$, where $\dagger$ denotes Hermitian conjugation, upon transition from the continuous to the discrete case, the matrix representations of the total momentum operators for our $4n^2$-dimensional eigenvectors $\Phi^{(i)}$ are $\mathsf{J}_i = \mathbb{I}_{n^2} \otimes \mathsf{j}_i$ where $\mathbb{I}_{n^2}$ is the $n^2 \times n^2$ identity matrix

$$\mathsf{J}_x = \begin{pmatrix} \mathsf{j}_x & 0 & \cdots & 0 \\ 0 & \mathsf{j}_x & \ddots & \vdots \\ \vdots & \ddots & \ddots & 0 \\ 0 & \cdots & 0 & \mathsf{j}_x \end{pmatrix}, \quad \mathsf{J}_y = \begin{pmatrix} \mathsf{j}_y & 0 & \cdots & 0 \\ 0 & \mathsf{j}_y & \ddots & \vdots \\ \vdots & \ddots & \ddots & 0 \\ 0 & \cdots & 0 & \mathsf{j}_y \end{pmatrix},$$
$$\mathsf{J}_z = \begin{pmatrix} \mathsf{j}_z & 0 & \cdots & 0 \\ 0 & \mathsf{j}_z & \ddots & \vdots \\ \vdots & \ddots & \ddots & 0 \\ 0 & \cdots & 0 & \mathsf{j}_z \end{pmatrix}. \tag{9}$$

We find that each state is doubly degenerate such that any linear combination is also an eigenstate with the same eigenenergy. To find the states of definite angular momentum $\langle J_i \rangle$ we lift the degeneracy by adding a *very* small electric field across the wire, large enough to break the degeneracy but small enough not to affect the energies significantly. The perturbation to the Hamiltonian takes the form $H \rightarrow H + \delta H$ where $\delta H = -V_0(y + \frac{1}{2}z)$, with V_0 small (of the order 10^{-9}eV), and a factor of $\frac{1}{2}$ so that the degeneracy is lifted differently in y and z.

3. Results

3.1. Dispersion relations

The band structure for various cross sections having quantised in the $\hat{\mathbf{y}}$ and $\hat{\mathbf{z}}$ can be found in figure 2. For smaller values of L, the bands approximately take the form of hyperbolae. For larger cross-sections, however, we see some anticrossing near the gamma point induced by spin–orbit coupling (SOC) which is characteristic of TIs. This is consistent with the *ab initio* calculations of Zhang *et al* [32] for Bi_2Se_3. The SOC shifts the electron subbands down in energy and the hole subbands up, forcing the subbands to anticross. Without anticrossing, the band structure would presumably be a set of intersecting hyperbolae. This results in *nonmonotonic* bands with points of inflexion where $\mathrm{d}^2\epsilon/\mathrm{d}k_x^2 = 0$. At these inflexion points the electrons and holes have a divergent effective mass $m^* = \hbar^2(\mathrm{d}^2\epsilon/\mathrm{d}k_x^2)^{-1}$. Far away from $\epsilon = 0$, the bands return to being approximately hyperbolic. Even the bands near $\epsilon = 0$ are linear away from $k_x = 0$ where the electron and hole subbands are well separated. For 15 QL in figure 3(b) we see some 'unexpected' electron subbands with a lower curvature (at least as $k_x \rightarrow 0$, that is). These do not correspond to surface states—they are bulk states which so happen to have a low enough energy to appear within the pictured energy range.

We quote the result derived by Brey and Fertig [33] who give an analytic expression for the dispersion relation under the assumption that $M_1 = M_2 = \epsilon(\mathbf{k}) = 0$, such that the Hamiltonian exhibits particle hole symmetry

$$E_{n,k_x} = \pm\sqrt{(A_0 k_x)^2 + \left[\pi \frac{A_0 B_0}{A_0 L_y + B_0 L_z}\left(n - \tfrac{1}{2}\right)\right]^2} \tag{10}$$

where $n = 1, 2, 3, \ldots$. For $k_x = 0$ and $L_z = L_y = L$ equation (10) reduces to the simple expression

$$E_n = \pm\pi \frac{A_0 B_0}{(A_0 + B_0)L}\left(n - \tfrac{1}{2}\right) \equiv \pm\Delta E_{\mathrm{a}}\left(n - \tfrac{1}{2}\right) \tag{11}$$

which defines the analytic energy gap ΔE_{a}. We compare the energy gaps observed in our numerically calculated dispersion relations against this analytic result. For our numerical results we define $\Delta E_n \equiv E_{n+1} - E_n$ such that the topmost hole subband is given an index of $n = 0$ and hence the band gap is given by ΔE_0. We see from figure 2 that equation (11) gets the salient features of the dispersion relations correct. Away from $\epsilon = 0$, the bands are approximately hyperbolae. For each value of L the ratio $\Delta E_0/\Delta E_{\mathrm{a}}$ is of order $\mathcal{O}(1)$ and the energy gaps ΔE_n, at least for larger values of L, remain approximately constant.

When quantising instead in x and y we produce a different set of dispersion relations, which can be found in figure 3, as we expected since the crystal structure and thus (2) are not isotropic. The bands are, for *all* values of L, approximately hyperbolic, but only for larger values of L are the states equally spaced in energy, and hence consistent with the analytic results derived by Brey and Fertig in [33]. The electron and hole subbands are sufficiently well separated in energy for there to be no anticrossing. For smaller cross sections the dispersion relation is interrupted by low-energy bulk states.

As we traverse the band structure upwards, *i.e.* the order of the electron subbands $N = 1, 2, 3, \ldots$, we see that the number of nodes in $|\Phi|^2$ in the *horizontal* ($\hat{\mathbf{y}}$) direction increases as $N - 1$, that is 0, 1, 2, …. This is a well known result in quantum mechanics. For each state in figure 4 there exists a degenerate partner related to those shown by a mirror flip in the line $y = L/2$ in accordance with the symmetry of the crystal—the states must respect the *inversion*

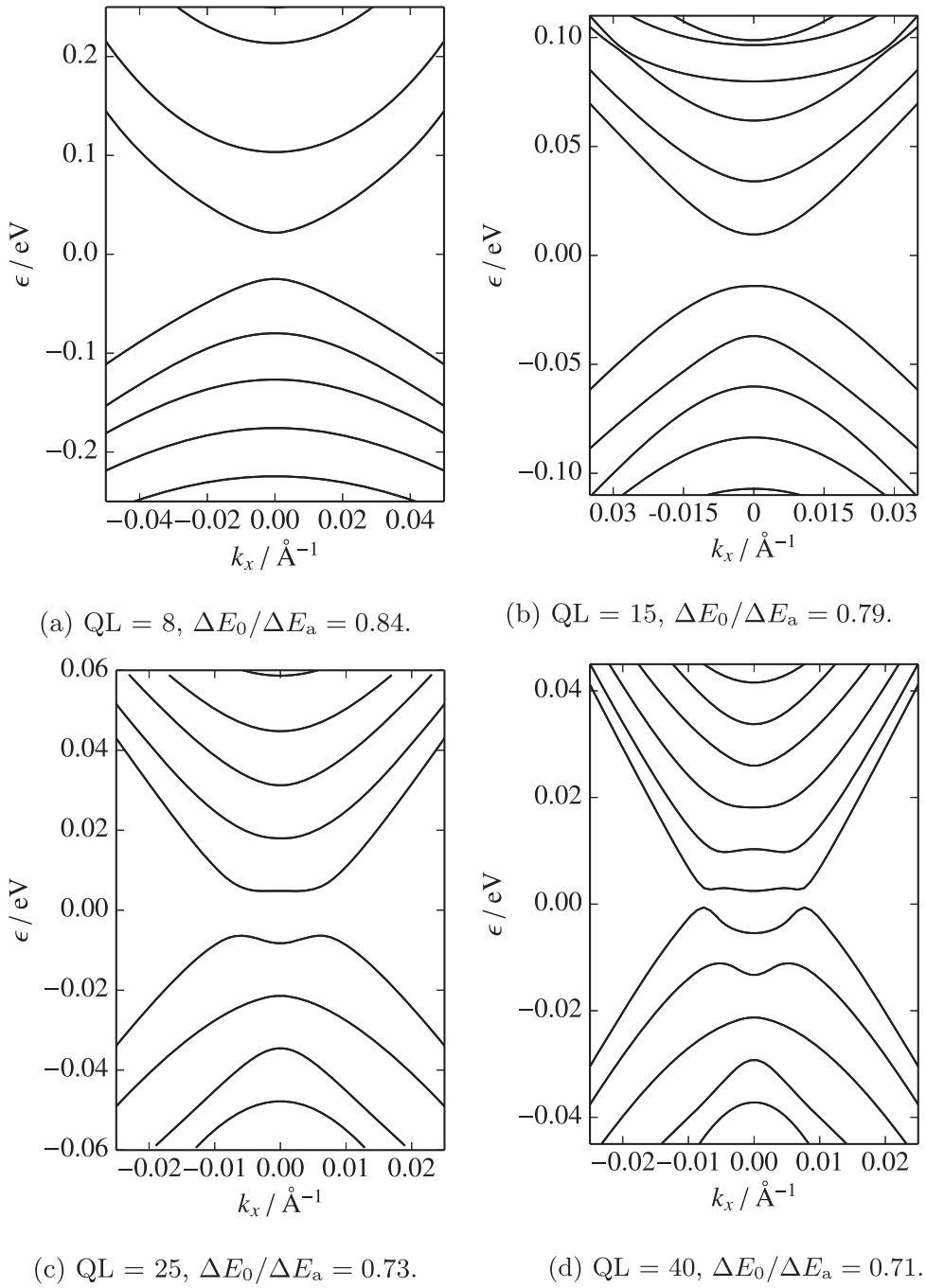

Figure 2. Band structure for various cross sections in the *y*-*z* plane. For larger values of L the effect of SOC becomes more pronounced and the electron and hole subbands are forced together. The bands have been shifted in energy such that the centre of the band gap lies at $\epsilon = 0$.

symmetry (about $\mathbf{r} = (0, L/2, L/2)$) exhibited by the crystal and so one edge should not be favoured. We lifted the degeneracy between these two states by perturbing the Hamiltonian $H \to H + \delta H$ with $\delta H = -V_0(y + \frac{1}{2}z)$ and V_0 small. For the hole subbands and $k_x = 0.0125$ Å we see an increasing number of nodes but in the *vertical* ($\hat{\mathbf{z}}$) direction. As for the electron subbands there exists a degenerate partner related via symmetry with opposite spin.

3.2. Surface states

We plotted the wavefunctions with Matlab using Delaunay triangulation (`delaunay(x, y)`) and interpolated shading (Figures 5, 6). For every cross section the states near the Γ point and the zero in energy are *surface states*. Quantising in x and y, the states have a smaller penetration depth in the $\hat{\mathbf{z}}$ direction than in the $\hat{\mathbf{y}}$ direction, but the wavefunction along the y edges ($z = 0, L$) has a greater magnitude. At the corners of the domain, 'constructive interference' between the two surfaces at the y and z edges causes a peak in each corner. Taking a quadrant ($\mathcal{A}$ defined by, say, $y > L/2$ and $z > L/2$) of the domain we may deduce whether an electron is more

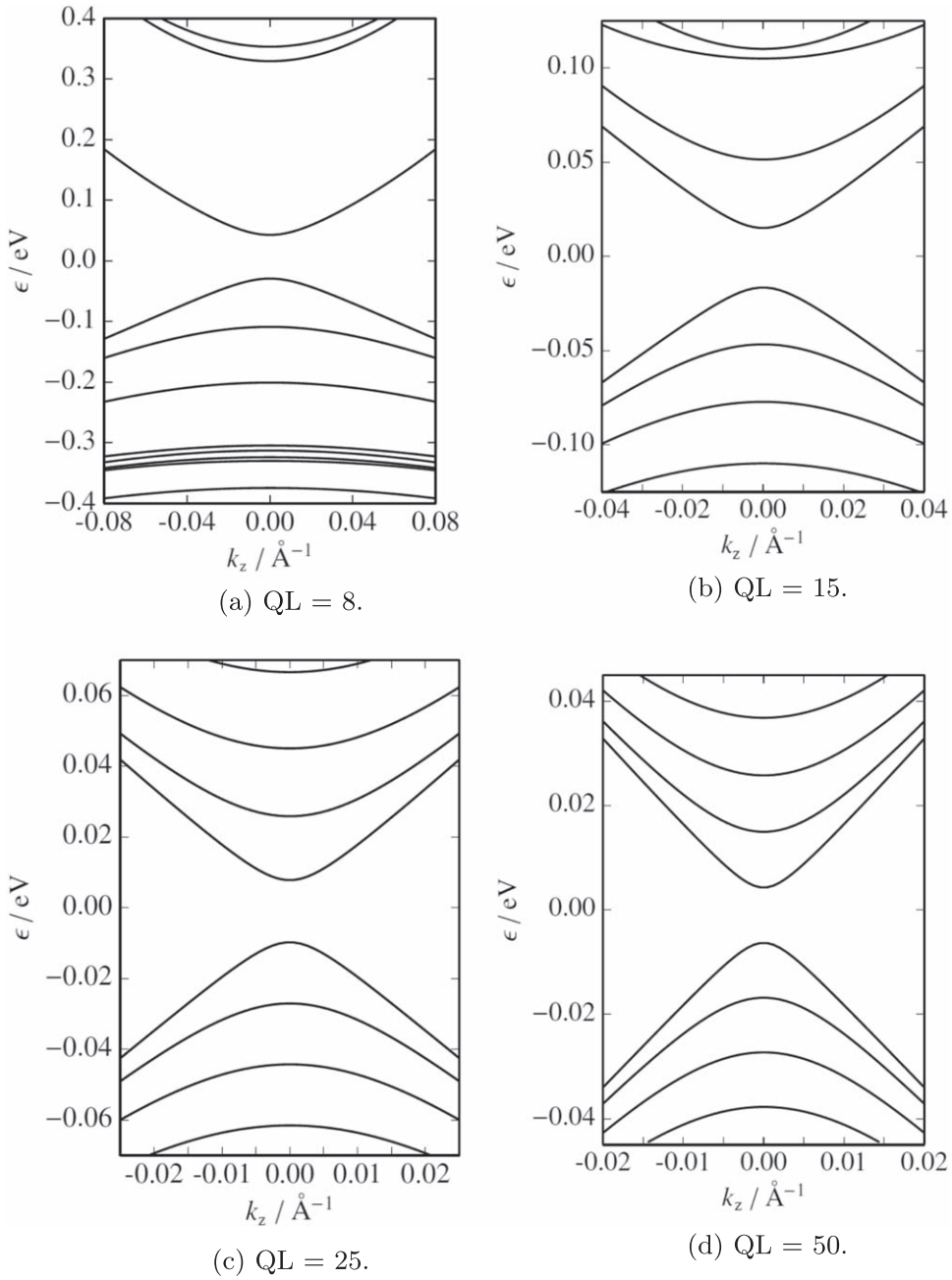

Figure 3. Band structure for various cross sections in the *x*-*y* plane. The band structure now exhibits no anticrossing.

likely to be found along a *z* or a *y* surface by splitting the quadrant in two along its diagonal (the line $y = z$) and evaluating $\iint_{\mathcal{A}} |\Phi|^2 \, \mathrm{d}^2\mathbf{r}$. For 25 QL it turns out that it is more probable for an electron to be found along the *y* edge (53%), while for 40 QL the *z* edge is more likely.

When quantising instead in k_x and k_y, the surface states exhibit a much greater degree of symmetry, but otherwise contain the same features. For 8 QL (and below), the states from both surfaces overlap to produce a non-zero amplitude at the centre of the wire. To find the corresponding penetration depth we must discretise an inner product along a thin strip of surface at the edge in order to calculate the expectation value of *y* from our states $\Phi^{(i)}$, namely

$$\langle \hat{y} \rangle = \frac{\langle \Phi | \hat{y} | \Phi \rangle}{\langle \Phi | \Phi \rangle} \equiv \frac{\iint_{\mathcal{S}} y \Phi^{\dagger}(\mathbf{r}) \Phi(\mathbf{r}) \, \mathrm{d}^2\mathbf{r}}{\iint_{\mathcal{S}} \Phi^{\dagger}(\mathbf{r}) \Phi(\mathbf{r}) \, \mathrm{d}^2\mathbf{r}} \rightarrow \frac{\sum_i \sum_j ih \cdot h^2 \Phi^{\dagger}_{i,j} \Phi_{i,j}}{\sum_i \sum_j h^2 \Phi^{\dagger}_{i,j} \Phi_{i,j}}, \tag{12}$$

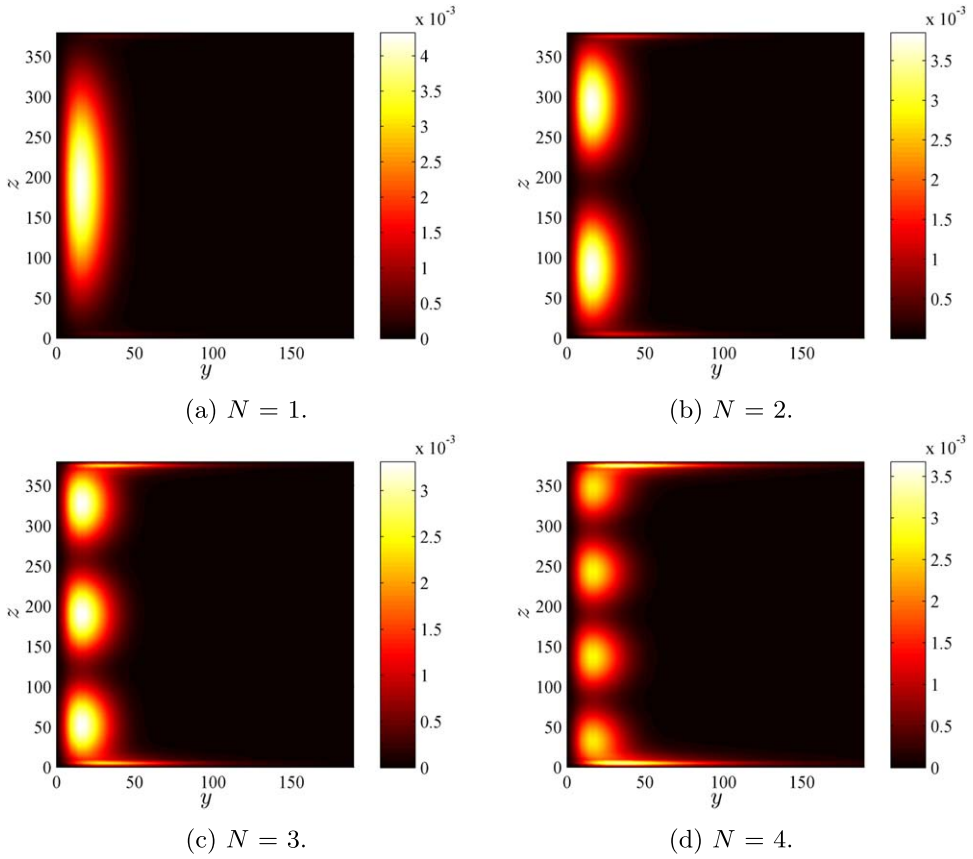

Figure 4. Cross sections of wires, 40QL by 80QL. $|\Phi|^2$ for various electron subband orders and $k_x = 0.0125$ Å^{-1}. We observe an increasing number of *horizontal* nodes in the wavefuction with increasing N.

where Φ is the *unnormailsed* wavefunction and $h = L/(n+1)$ is the distance between adjacent lattice sites. A similar expression exists for $\langle \hat{z} \rangle$ with the substitution $ih \rightarrow jh$. This expression in most appropriate for states which possess little symmetry about the centre of the cross section. However, a more appropriate measure of penetration depth for a more symmetrical wavefunction is the difference between the width L and the root mean square deviation from the centre, $\ell_y \equiv L - \sqrt{\langle (\hat{y} - L/2)^2 \rangle}$ and

$$(L - \ell_y)^2 = \frac{\langle \Phi | \, (\hat{y} - L/2)^2 \, | \Phi \rangle}{\langle \Phi | \Phi \rangle} \rightarrow \frac{\sum_i \sum_j (ih - L/2)^2 \cdot h^2 \Phi^\dagger_{i,j} \Phi_{i,j}}{\sum_i \sum_j h^2 \Phi^\dagger_{i,j} \Phi_{i,j}}. \tag{13}$$

where again the relationship for ℓ_z is obtained by making the substitution $ih \rightarrow jh$. For a symmetrical surface state equation (12) would give a penetration depth of zero.

For the bottommost electron subband, ($N = 1$), we look at the effect of increasing k_x on the wavefunctions. Counter-intuitively, the penetration depth $\langle \hat{y} \rangle$ (these states are not symmetric) *increases* with increasing k_x. *If* k_x were representative of the system's total kinetic energy, one would expect the states to exhibit greater curvature ($\nabla^2 \Phi$), and thus a smaller penetration depth. Resorting to classical reasoning, it is possible that increasing the system's momentum in the $\hat{\mathbf{x}}$ direction ($\hbar k_x$) results in increased penetration depth as SOC may be represented by an effective magnetic field, which gives rise to a Lorentz force $\mathbf{F} = -e(\mathbf{v} \wedge \mathbf{B})$, which acts towards the centre of the wire. We plot $\langle y \rangle$ against k_x in figure 7 for 25 and 50 QL.

3.3. Spin and angular momentum

The expectation value of the angular momentum operators $\hat{J}_x$ and $\hat{J}_y$, $\langle \hat{J}_x \rangle$ and $\langle \hat{J}_y \rangle$, are plotted as vectors on top of the dispersion relation in figures 8 and 9. The expectation of the ith spin operator $\langle \hat{s}_i \rangle = 0$ ($i \neq 2$), that is, the spin of the states lies solely in the y direction. Since $[H, \mathcal{T}] = 0$, where $\mathcal{T} = -\mathrm{i}\sigma_2 \mathcal{K}$ and $\mathcal{K}$ is the complex conjugate operator, the system preserves time reversal symmetry. This implies the existence of Kramer's pairs *i.e.* energy levels are doubly degenerate with states at $\mathbf{k}$ and $-\mathbf{k}$ [1] with opposite spins. For each energy eigenvalue there exist two states, one with $\langle \hat{J}_y \rangle > 0$ and another with $\langle \hat{J}_y \rangle < 0$, with positive and negative

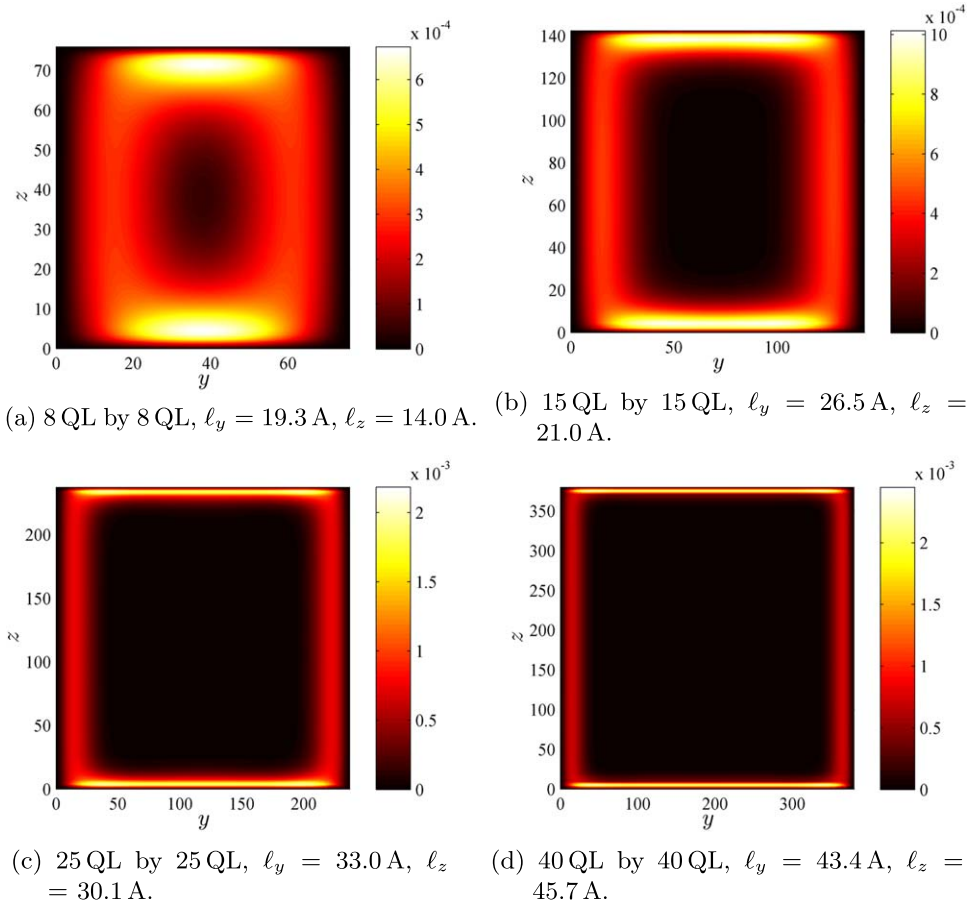

(a) 8 QL by 8 QL, $\ell_y = 19.3$ A, $\ell_z = 14.0$ A. (b) 15 QL by 15 QL, $\ell_y = 26.5$ A, $\ell_z = 21.0$ A.

(c) 25 QL by 25 QL, $\ell_y = 33.0$ A, $\ell_z = 30.1$ A. (d) 40 QL by 40 QL, $\ell_y = 43.4$ A, $\ell_z = 45.7$ A.

Figure 5. $|\Phi|^2$ over $\mathcal{S}$ (quantized in k_y and k_z) for (unnormalised) first electron surface states and $k_x = 0$. For larger values of L the penetration depth as a fraction of the total width decreases, while the *absolute* value of the penetration depth increases.

eigenvalues having the same magnitude. With inversion $\mathbf{k} \rightarrow -\mathbf{k}$ the energy ordering of these two states is reversed(when the degeneracy is lifted). The degeneracy can be observed in figures 8 and 9, where each band is symmetric under inversion $k_x \rightarrow -k_x$. Had we not lifted the degeneracy of these states using a linear electric field, we would have obtained random linear combinations of both degenerate states. This degeneracy is an example of Kramer's pairs.

3.4. Ballistic conduction

Following Moroz and Barnes [34], we now use our dispersion relations to calculate the *Ballistic Conductance* G of a long Q1DES at low temperature (Figures 10, 11).

$$G(\epsilon_F) = \frac{e^2}{h} M(\epsilon_F) \equiv G_0 M(\epsilon_F) \tag{14}$$

where ϵ_F is the Fermi energy and $M(\epsilon_F)$ is the number of occupied electron subbands. $M(\epsilon_F)$ is given by

$$M(\epsilon_F) = \sum_n \sum_i \sum_{s=\uparrow,\downarrow} \theta(\epsilon_F - \epsilon^s_{\min}(n, i)) \tag{15}$$

where $\theta(x)$ is the unit step function and $\epsilon^s_{\min}(n, i)$ represents the energy of the ith minimum of the nth subband. We assume that equation (14) holds true which necessitates conservation of (charge) current $\mathbf{j}$. Moroz and Barnes in [34] proved that current is indeed conserved in the presence of finite SOC. To find G from equation (14) one needs only to draw a horizontal line for each Fermi energy and count the number of intersections with the band structure which gives the value of G in units of G_0.

We found in section 3.1 that for larger widths L the dispersion relations exhibit points of inflexion. The current passing through a 1D subband is not affected by the diverging effective mass when there is no scattering mechanism [34]. However between the two points of inflexion there exist regions where $v_x = \hbar^{-1}(\mathrm{d}\epsilon/\mathrm{d}k_x) < 0$ for $k_x > 0$ and, equivalently, $v_x > 0$ for $k_x < 0$. This *does* significantly affect $G(\epsilon)$ since both forward and backward travelling electron modes contribute and we see a corresponding peak in $G(\epsilon)$. As we move further away from $\epsilon = 0$ where SOC becomes increasingly negligible, the points of inflection disappear along with the

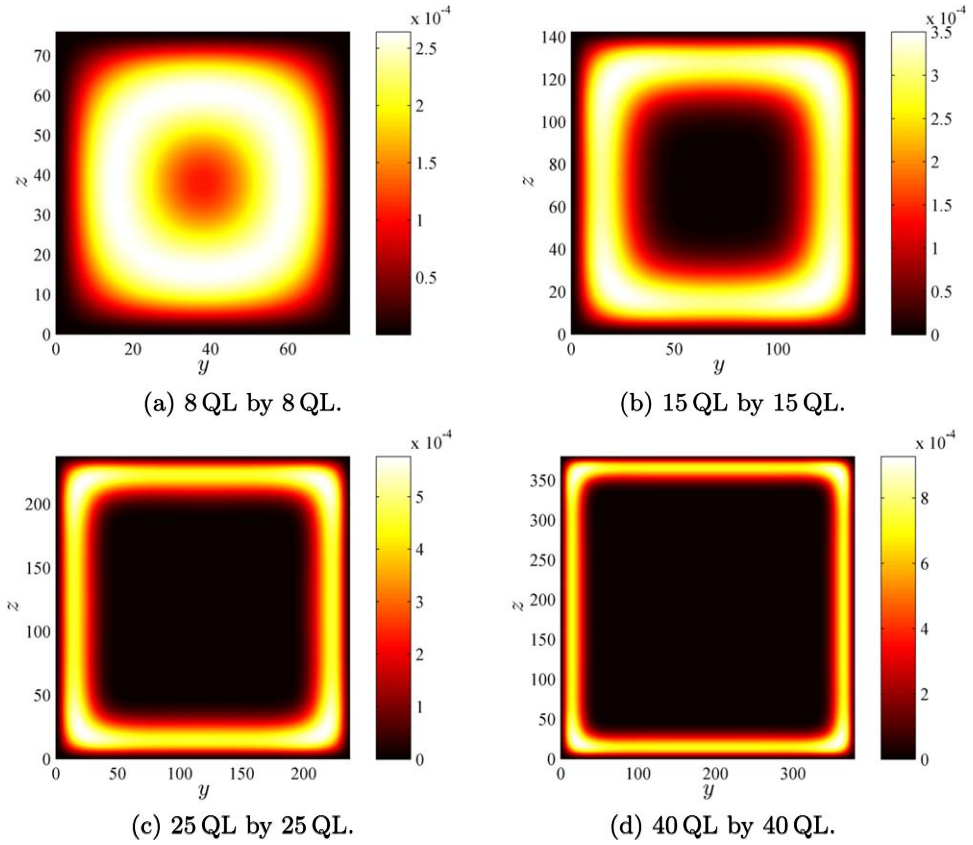

Figure 6. $|\Phi|^2$ over $\mathcal{S}'$ (quantized in k_x and k_y) for (unnormalised) first electron surface states and $k_z = 0$. For larger values of L the penetration depth as a fraction of the total width decreases, while the *absolute* value of the penetration depth increases.

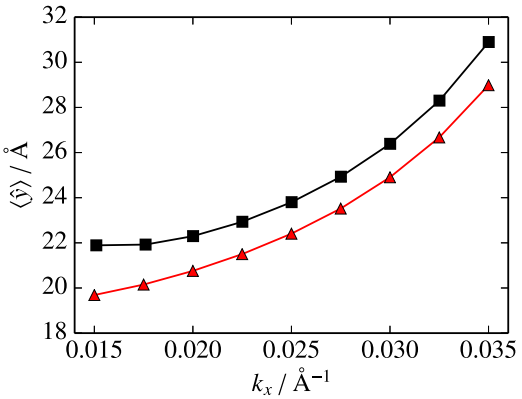

Figure 7. Penetration depth $\langle \hat{y} \rangle$ versus k_x for 25 QL (black squares) and 50 QL (red triangles). In both cases (over the pictured range) the penetration depth increases monotonically with k_x.

regions over which the group velocity is negative and no peak in $G(\epsilon)$ is observed. This is also the case for smaller values of L where the effect of SOC is not sufficiently strong.

4. Conclusions

We have found using numerical techniques the band structure and wavefunctions for Bi_2Se_3 TI quantum nanowires of square cross section. Quantising in y and z we observed anticrossing *non-monotonic* bands for larger widths than previous analytic analyses; far away from the gap, the bands return to being approximately hyperbolic. Quantising instead in the more symmetrical x and y we observed well separated hyperbolic, *monotonic* bands, consistent with previous literature [33].

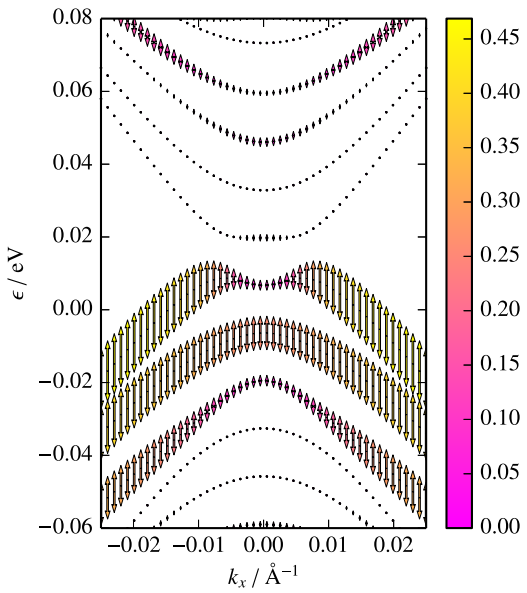

Figure 8. 25 QL. Dispersion relations with expectation of $\langle \hat{J}_{x(y)} \rangle$ overlaid. The colourmap represents the magnitude of expectation $|\langle \hat{J}_y \rangle|$.

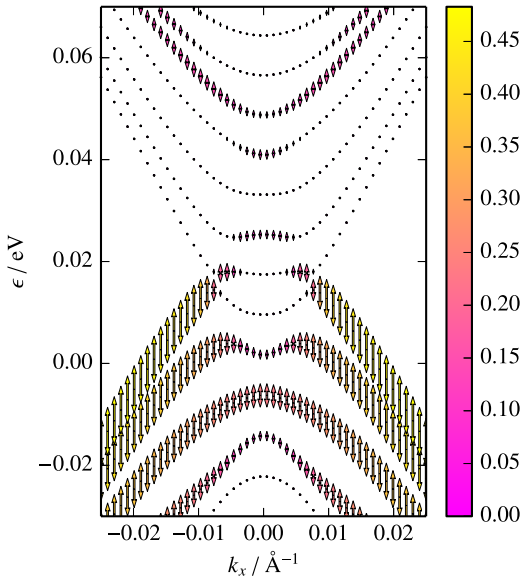

Figure 9. 40 QL. Dispersion relations with expectation of $\langle \hat{J}_{x(y)} \rangle$ overlaid. The colourmap represents the magnitude of expectation $|\langle \hat{J}_y \rangle|$.

We observed the change in the wavefunction with electron subband order for some fixed k and found it exhibits increasing numbers of nodes with increasing subband order, as might be expected from standard quantum mechanics. For *all* possible quantisations we found surface states near the Γ point, whose penetration depth *increases* with increasing wavenumber. We observed constructive interference between surface states at the device corners, and showed that the electron's 'preferred' edge (namely, the one with the higher probability density) changes with wire dimension in the case where the wire cross-section directions are along the y- and z- directions of the crystal.

In addition to investigating the energetic structure and penetration depth of the surface states of the TI, we have also discussed the impact on the ballistic conductance of a Q1DES. We used the conservation of current in the presence of finite SOC to calculate the ballistic conductance G of a long TI nanowire directly from the energy spectrum, using the Landauer formula, and observed peaks in $G(\epsilon)$ due to points of inflexion in the bandstructure. We made some predictions about the location and magnitude of these peaks compared to a usual

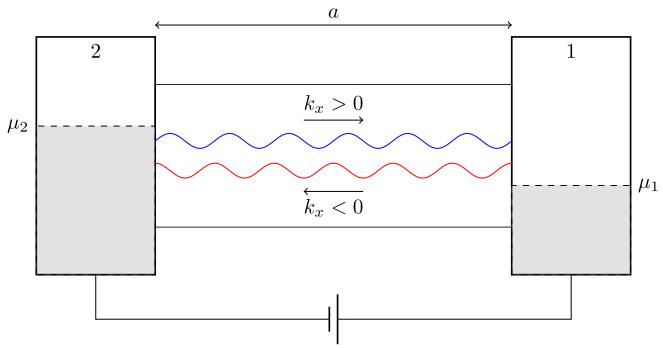

Figure 10. Cartoon of a nanowire set up to exhibit ballistic conductance. Forward travelling modes with $k_x > 0$ carry electrons from the left contact to the right and the backward travelling modes with $k_x < 0$ vice versa since the contacts are assumed to be reflectionless.

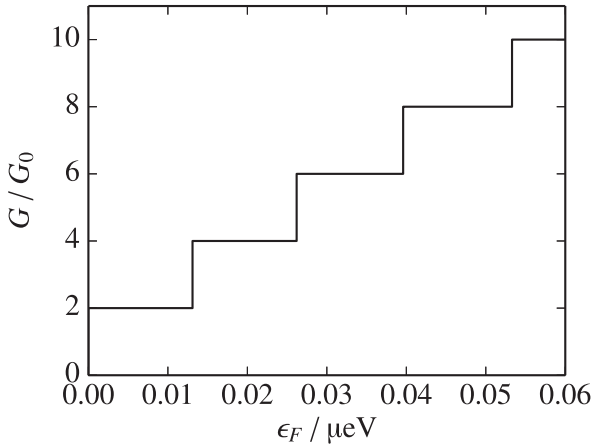

(a) Square cross section with $L = 25$ QL. G jumps up in steps of $2G_0$ at points equally spaced in energy.

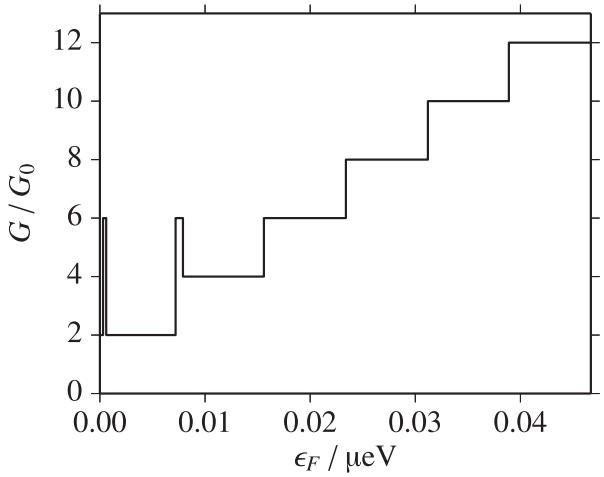

(b) $L = 25$ QL. For electron subbands with low $N = 1, 2$, the points of inflexion in the dispersion relation cause jumps in G of height $2G_0$.

Figure 11. Ballistic conduction of Bi_2Se_3 for various cross-sections.

quantised conductance measurement. The work done in this paper, particularly on the subject of conduction, is relevant to potential experimental probes such as those in [35, 36].

It is important to note that the Liu Hamiltonian, used through this paper, is derived from crystal symmetries with parameters from $k \cdot p$ theory fitted to *ab initio* calculations. Thus, results derived using such a Hamiltonian should carry over to a lesser or greater extent to any crystal with similar symmetry. This gives our results some

generalisabilty into the wider field of topological insulators of the same family as Bi_2Se_3, where the quantitative results will vary depending on the value of the fitting parameters but the qualitative observations should hold (with the natural exception of the class of trivial insulators also modelled by a Hamiltonian of the Liu form but where the band inversion criterion $M_0 M_1 < 0$ is not met [29]).

Acknowledgments

The work of A N was supported by the EPSRC. The authors would like to extend their thanks to Oliver Hart for calculations that supported this paper.

Appendix A. Derivation of the Liu Hamiltonian

The following is a summary of work done by Liu *et al* [29]. $Bi_2 Se_3$ has a layered structure, with each layer consisting of Be or Si atoms arranged in hexagonal lattices which are stacked in the *A-B-C-A-B-C-*…configuration. The unit cell contains five atoms total with two equivalent Se atoms (labelled Se1 and Se1′) and two equivalent Be atoms (Be1 and Be1′). Each set of 5 layers is known as a quintuple layer (QL) with 1 QL $\approx$ 9.5 Å. Strong chemical bonds hold together atoms within one QL, while adjacent QLs are held together by weak Van der Waals forces, so only the bonding within one QL is considered first. The hybridised atomic states associated with Bi and Bi′ ($|B_\alpha\rangle$, $|B'_\alpha\rangle$ respectively), and Se and Se′ ($|S_\alpha\rangle$, $|S'_\alpha\rangle$ respectively) are combined to form states with parity eigenvalues ± 1 (upper index)

$$|P1^{\pm},\, \alpha\rangle = \tfrac{1}{\sqrt{2}}(|B_\alpha\rangle \mp |B'_\alpha\rangle) \tag{16}$$

$$|P2^{\pm},\, \alpha\rangle = \tfrac{1}{\sqrt{2}}(|S_\alpha\rangle \mp |S'_\alpha\rangle) \tag{17}$$

where $\alpha = p_x, p_y, p_z$. $|P1^-,\, \alpha\rangle$ and $|P2^+,\, \alpha\rangle$ are too far away from the Fermi energy to give a significant contribution to wavefunctions and so are neglected from this point onwards. We now introduce a basis formed of the eigenstates of the angular momentum operator $\hat{L}_z$ and include spin $\sigma = \uparrow, \downarrow$. Up to this point, the $\uparrow$ and $\downarrow$ states have been degenerate. Clearly $|P1^+,\, p_z,\, \sigma\rangle$ and $|P2^-,\, p_z,\, \sigma\rangle$ are already eigenstates of $\hat{L}_z$ with eigenvalues 0, whereas we must form superpositions of the other states

$$|\Lambda,\, p_+,\, \sigma\rangle = -\tfrac{1}{\sqrt{2}}(|\Lambda,\, p_x,\, \sigma\rangle + \mathrm{i}|\Lambda,\, p_y,\, \sigma\rangle) \tag{18}$$

$$|\Lambda,\, p_-,\, \sigma\rangle = \tfrac{1}{\sqrt{2}}(|\Lambda,\, p_x,\, \sigma\rangle - \mathrm{i}|\Lambda,\, p_y,\, \sigma\rangle) \tag{19}$$

where $\Lambda = P1^+,\, P2^-$, such that (18) has the eigenvalue $+\hbar$ and (19) $-\hbar$. The Hamiltonian $\hat{H} + \hat{H}_{\mathrm{SO}} = \hat{H} + \lambda \hat{\mathbf{L}} \cdot \hat{\mathbf{s}}$, with $\lambda = (2m_0^2 c^2 r)^{-1} \partial U / \partial r$, which now includes spin–orbit coupling, is expressed in the basis of the 12 remaining states. The matrix is block diagonal and so may be diagonalised by individually diagonalising each block. We require the solution to the eigenvector problem defined by the matrix

$$\begin{pmatrix} E_{\Lambda,x} - \lambda_\Lambda/2 & \lambda_\Lambda/\sqrt{2} \\ \lambda_\Lambda/\sqrt{2} & E_{\Lambda,z} \end{pmatrix}, \tag{20}$$

where $\lambda_\Lambda/2 \equiv \langle \Lambda,\, p_+,\, \uparrow |\hat{H}_{\mathrm{SO}}| \Lambda,\, p_+,\, \uparrow \rangle$. This matrix has 2 eigenvectors given by

$$\begin{pmatrix} u_\pm^\Lambda \\ v_\pm^\Lambda \end{pmatrix} = \frac{1}{N_\pm} \begin{pmatrix} \Delta E_\Lambda \pm \sqrt{\Delta E_\Lambda^2 + \lambda_\Lambda^2/2} \\ \lambda_\Lambda/2 \end{pmatrix} \tag{21}$$

where $N \pm = \lambda_\Lambda^2 + 2\Delta E_\Lambda^2 \pm 2\Delta E_\Lambda \sqrt{\Delta E_\Lambda^2 + \lambda_\Lambda^2/2}$ and $\Delta E_\Lambda = (E_{\Lambda,x} - E_{\Lambda,z} - \lambda_\Lambda/2)/2$. Since ΔE_Λ and λ_Λ are real, $u_\pm^\Lambda$ and $v_\pm^\Lambda$ are real also. We obtain the new states which diagonalise the Hamiltonian with SOC included:

$$|\Lambda,\, \tfrac{3}{2}\rangle = |\Lambda,\, p_+,\, \uparrow\rangle \tag{22}$$

$$|\Lambda,\, -\tfrac{3}{2}\rangle = |\Lambda,\, p_-,\, \downarrow\rangle \tag{23}$$

$$|\Lambda_+,\, \tfrac{1}{2}\rangle = u_+^\Lambda |\Lambda,\, p_z,\, \uparrow\rangle + v_+^\Lambda |\Lambda,\, p_+,\, \downarrow\rangle \tag{24}$$

$$|\Lambda_-,\, \tfrac{1}{2}\rangle = u_-^\Lambda |\Lambda,\, p_z,\, \uparrow\rangle + v_-^\Lambda |\Lambda,\, p_+,\, \downarrow\rangle \tag{25}$$

$$|\Lambda_+,\, -\tfrac{1}{2}\rangle = u_+^\Lambda |\Lambda,\, p_z,\, \downarrow\rangle + v_+^\Lambda |\Lambda,\, p_+,\, \uparrow\rangle \tag{26}$$

$$|\Lambda_+,\, -\tfrac{1}{2}\rangle = u_-^\Lambda |\Lambda,\, p_z,\, \downarrow\rangle + v_-^\Lambda |\Lambda,\, p_+,\, \uparrow\rangle, \tag{27}$$

where the second index represents m_j i.e. $\hat{J}_z|\Lambda_{(\pm)}, m_j\rangle = m_j\hbar|\Lambda_{(\pm)}, m_j\rangle$. We take the model Hamiltonian proposed by Liu *et al* [29] which was derived using symmetry and given in terms of the basis states $|P1^+_-, \frac{1}{2}\rangle \equiv |1\rangle, |P2^-_+, \frac{1}{2}\rangle \equiv |2\rangle, |P1^+_-, -\frac{1}{2}\rangle \equiv |3\rangle$ and $|P2^-_+, -\frac{1}{2}\rangle \equiv |4\rangle$. These states were found to be closest to the Fermi energy and hence give the most significant contribution to the wavefunction.

Appendix B. Submatrices of the Hamiltonian

We define the following matrices

$$\mathcal{H}_0(k_x) = \begin{pmatrix} \Pi & 0 & 0 & \mathrm{i}A_0k_x \\ 0 & \Xi & \mathrm{i}A_0k_x & 0 \\ 0 & -\mathrm{i}A_0k_x & \Pi & 0 \\ -\mathrm{i}A_0k_x & 0 & 0 & \Xi \end{pmatrix}, \tag{28}$$

$$\mathcal{H}_1^{(y)} = \begin{pmatrix} 0 & 0 & 0 & -\mathrm{i}A_0 \\ 0 & 0 & -\mathrm{i}A_0 & 0 \\ 0 & -\mathrm{i}A_0 & 0 & 0 \\ -\mathrm{i}A_0 & 0 & 0 & 0 \end{pmatrix}, \tag{29}$$

$$\mathcal{H}_2^{(y)} = -\begin{pmatrix} C_2 + M_2 & 0 & 0 & 0 \\ 0 & C_2 - M_2 & 0 & 0 \\ 0 & 0 & C_2 + M_2 & 0 \\ 0 & 0 & 0 & C_2 - M_2 \end{pmatrix}, \tag{30}$$

$$\mathcal{H}_1^{(z)} = \begin{pmatrix} 0 & -B_0 & 0 & 0 \\ B_0 & 0 & 0 & 0 \\ 0 & 0 & 0 & -B_0 \\ 0 & 0 & B_0 & 0 \end{pmatrix}, \tag{31}$$

$$\mathcal{H}_2^{(z)} = -\begin{pmatrix} C_1 + M_1 & 0 & 0 & 0 \\ 0 & C_1 - M_1 & 0 & 0 \\ 0 & 0 & C_1 + M_1 & 0 \\ 0 & 0 & 0 & C_1 - M_1 \end{pmatrix}, \tag{32}$$

where $\Pi = C_0 + M_0 + (C_2 + M_2)k_x^2$ and $\Xi = C_0 - M_0 + (C_2 - M_2)k_x^2$. Then the matrices $\mathcal{C}_{\mu,\nu}$ are given by

$$\mathcal{C}_{0,0} = \mathcal{H}_0 - \tfrac{2}{h^2}(\mathcal{H}_2^{(y)} + \mathcal{H}_2^{(z)}) \tag{33}$$

$$\mathcal{C}_{\pm1,0} = \pm\tfrac{1}{2h}\mathcal{H}_1^{(y)} + \tfrac{1}{h^2}\mathcal{H}_2^{(y)} \tag{34}$$

$$\mathcal{C}_{0,\pm1} = \pm\tfrac{1}{2h}\mathcal{H}_1^{(z)} + \tfrac{1}{h^2}\mathcal{H}_2^{(z)} \tag{35}$$

Appendix C. Finite difference approximation

The finite difference approximation consists of the following substition:

$$\partial_j\Phi(\mathbf{r}) \to \frac{1}{h}(\Phi(\mathbf{r} + h\mathbf{j}) - \Phi(\mathbf{r} - h\mathbf{j})) \tag{36}$$

$$\partial_j^2\Phi(\mathbf{r}) \to \frac{1}{h^2}(\Phi(\mathbf{r} + h\mathbf{j}) - 2\Phi(\mathbf{r}) + \Phi(\mathbf{r} - h\mathbf{j})) \tag{37}$$

where $j = x, y, z$ labels the direction of differentiation and the vector $\mathbf{j}$ is the unit vector in that direction.

ORCID iDs

A Nikolic https://orcid.org/0000-0001-5784-0316

References

[1] Ando Y 2013 Topological insulator materials *J. Phys. Soc. Jpn.* **82** 102001
[2] Fu L, Kane C L and Mele E J 2007 Topological insulators in three dimensions *Phys. Rev. Lett.* **98** 106803
[3] Hasan M Z and Kane C L 2010 Colloquium: topological insulators *Rev. Mod. Phys.* **82** 3045
[4] Kane C L and Mele E J 2005 Quantum spin Hall effect in graphene *Phys. Rev. Lett.* **95** 226801

[5] Garate I and Glazman L 2012 Weak localization and antilocalization in topological insulator thin films with coherent bulk-surface coupling *Phys. Rev.* B **86** 035422
[6] Kim Y S, Brahlek M, Bansal N, Edrey E, Kapilevich G A, Iida K, Tanimura M, Horibe Y, Cheong S-W and Oh S 2011 Thickness-dependent bulk properties and weak antilocalization effect in topological insulator Bi_2Se_3 *Phys. Rev.* B **84** 073109
[7] Liu M *et al* 2012 Crossover between weak antilocalization and weak localization in a magnetically doped topological insulator *Phys. Rev. Lett.* **108** 036805
[8] Xia Y *et al* 2009 Observation of a large-gap topological-insulator class with a single Dirac cone on the surface *Nat. Phys.* **5** 398–402
[9] Zhang W, Yu R, Zhang H-J, Dai X and Fang Z 2010 First-principles studies of the three-dimensional strong topological insulators bi2te3, bi2se3 and sb2te3 *New J. Phys.* **12** 065013
[10] Hsieh D, Qian D, Wray L, Xia Y Q, Hor Y S, Cava R J and Hasan M Z 2008 A topological Dirac insulator in a quantum spin Hall phase *Nature* **452** 970–4
[11] Hsieh D *et al* 2009 A tunable topological insulator in the spin helical dirac transport regime *Nature* **460** 1101–5
[12] Hor Y S, Richardella A, Roushan P, Xia Y, Checkelsky J G, Yazdani A, Hasan M Z, Ong N P and Cava R J 2009 p-type bi 2 se 3 for topological insulator and low-temperature thermoelectric applications *Phys. Rev.* B **79** 195208
[13] Deb O, Soori A and Sen D 2014 Edge states of a three-dimensional topological insulator *J. Phys.: Condensed Matter* **26** 315009
[14] Seshadri R and Sen Confining D 2014 Dirac electrons on a topological insulator surface using potentials and a magnetic field *Phys. Rev.* B **89** 235415
[15] Bardarson J H and Moore J E 2013 Quantum interference and aharonov-bohm oscillations in topological insulators *Rep. Prog. Phys.* **76** 056501
[16] Zhu H, Zhao E, Richter C A and Li Q 2014 Topological insulator bi2se3 nanowire field effect transistors *ECS Transactions* **64** 51–9
[17] Cook A and Franz M 2011 Majorana fermions in a topological-insulator nanowire proximity-coupled to an s-wave superconductor *Phys. Rev.* B **84** 201105
[18] Dufouleur J *et al* 2017 Weakly-coupled quasi-1d helical modes in disordered 3d topological insulator quantum wires *Sci. Rep.* **7** 45276
[19] Erlingsson S I, Bardarson J H and Manolescu A 2018 Thermoelectric current in topological insulator nanowires with impurities *Beilstein Journal of Nanotechnology* **9** 1156
[20] Xypakis E, Rhim J-W, Bardarson J H and Ilan R 2017 Perfect transmission in rippled topological insulator nanowires arXiv:1712.06478
[21] Bernevig B A, Hughes T L and Zhang S-C 2006 Quantum spin Hall effect and topological phase transition in HgTe quantum wells *Science* **314** 1757–61
[22] König M, Wiedmann S, Brüne C, Roth A, Buhmann H, Molenkamp L W, Qi X-L and Zhang S-C 2007 Quantum spin Hall insulator state in HgTe quantum wells *Science* **318** 766–70
[23] König M, Buhmann H, Molenkamp L W, Hughes T, Liu C-X, Qi X-L and Zhang S-C 2008 The quantum spin Hall effect: theory and experiment *J. Phys. Soc. Jpn.* **77** 031007
[24] Zhou B, Lu H-Z, Chu R-L, Shen S-Q and Niu Q 2008 Finite size effects on helical edge states in a quantum spin-Hall system *Phys. Rev. Lett.* **101** 246807
[25] Liu C-X, Qi X-L, Zhang H J, Dai X, Fang Z and Zhang S-C 2010 Model Hamiltonian for topological insulators *Phys. Rev.* B **82** 045122
[26] Zhang H, Liu C-X, Qi X-L, Dai X, Fang Z and Zhang S-C 2009 Topological insulators in Bi_2Se_3, Bi_2Te_3 and Sb_2Te_3 with a single Dirac cone on the surface *Nat. Phys.* **5** 438
Shan W-Y, Lu H-Z and Shen S-Q 2010 Effective continuous model for surface states and thin films of three-dimensional topological insulators *New J. Phys.* **12** 043048
[28] Linder J, Yokoyama T and Sudbø A 2009 Anomalous finite size effects on surface states in the topological insulator Bi_2Se_3 *Phys. Rev.* B **80** 205401
[29] Liu C-X, Qi X-L, Zhang H, Dai X, Fang Z and Zhang S-C 2010 Model Hamiltonian for topological insulators *Phys. Rev.* B **82** 045122
[30] Fornberg B 1988 Generation of finite difference formulas on arbitrarily sized grids *Math. Comput.* **51** 699-706
[31] CenterSpace Software. NMath Premium 6.1, 2015.
[32] Zhang H, Liu C-X, Qi X-L, Dai X, Fang Z and Zhang S-C 2009 Topological insulators in bi2se3, bi2te3 and sb2te3 with a single dirac cone on the surface *Nat. Phys.* **5** 438
[33] Brey L and Fertig H A 2013 Electronic states of wires and slabs of topological insulators: quantum hall effects and edge transport *Phys. Rev.* B **89** 085305
[34] Moroz A V and Barnes C H W 1999 Effect of the spin-orbit interaction on the band structure and conductance of quasi-one-dimensional systems *Phys. Rev.* B **60** 14272
[35] Dufouleur J *et al* 2013 Quasiballistic transport of dirac fermions in a bi 2 se 3 nanowire *Phys. Rev. Lett.* **110** 186806
[36] Kong D, Randel J C, Peng H, Cha J J, Meister S, Lai K, Chen Y, Shen Z-X, Manoharan H C and Cui Y 2009 Topological insulator nanowires and nanoribbons *Nano Lett.* **10** 329–33